Extreme recharge triggers seismicity in a confined karst aquifer in southern Spain

Pedrera, A. [1]; García-Senz, J. [1]; González-Ramón, A. [1]; Gómez-Fontalva, J.M. [1]; Ruíz-Constán, A. [1]; Martos-Rosillo, S. [1]

1. Instituto Geológico y Minero de España. Consejo Superior de Investigaciones Científicas (IGME-CSIC), Madrid, Spain

This manuscript has been posted as a non-peer-reviewed preprint on EarthArXiv and is currently under review.

Abstract

Hydrological forcing during extreme recharge events can perturb crustal stress and trigger seismicity in a critically stressed crust, yet the coupling between aquifer dynamics and the spatio-temporal distribution of earthquake swarms remains poorly constrained. Here we document such a response during an exceptional rainfall episode in early 2026 that affected a confined karst aquifer in southern Spain.

Seismicity displays a coherent spatio-temporal evolution within the aquifer, from localized nucleation to distributed activation and outward migration, consistent with diffusion-driven pressure propagation through a connected fracture network. Stress modelling indicates that modest pore-pressure perturbations of ~0.4–0.7 MPa, comparable to decades of tectonic loading in the region, are sufficient to trigger slip on optimally oriented faults.

In addition to this dominant shallow seismicity, a subsidiary population of deeper earthquakes occurs within the underlying basement, exhibiting a systematic delay of ~4 days relative to shallow events. The delayed occurrence of basement seismicity is consistent with stress transfer from hydrologically driven shallow activity, indicating mechanical coupling between the two depth domains.

These results demonstrate that confined karst systems can act as transient stress modulators, controlling the timing and spatial organization of seismicity. As the frequency of extreme hydrological events increases, such systems may play a broader role in regulating shallow earthquake activity in tectonically active regions.

Keywords: Karst aquifer; Hydrological triggering; Earthquake swarms; Pore-pressure diffusion; Fault reactivation; Hydro-mechanical coupling.

1. Introduction

Hydrological processes perturb crustal stress and can trigger seismicity in tectonically active regions. Increases in pore pressure reduce effective normal stress on faults and promote failure, as described by classical Coulomb mechanics (e.g. Scholz, 2010; Wang and Manga, 2021; Shapiro et al., 2003). Numerous studies document temporal associations between intense precipitation and shallow earthquakes, indicating that transient hydrological loading can advance failure on critically stressed faults (e.g., Wolf, et al., 1997; Jiménez et al., 2000; Saar and Manga, 2003; Kraft et al., 2006; Hainzl et al., 2007; Husen et al., 2007; Bettinelli et al., 2008; Hsu et al., 2025).

Karst aquifers are characterized by high fracture connectivity and elevated hydraulic conductivities enabling rapid recharge and large-amplitude groundwater fluctuations. Earthquake occurrence has been linked to periods of maximum karst recharge (Bragato, 2021) and to seasonal groundwater loading that modulates crustal strain and seismicity (Tarantino et al., 2024), indicating that hydrological forcing can directly influence fault stability.

Despite this growing evidence, quantitative constraints on the stress perturbations generated by short-duration recharge events and rapid, high-amplitude water-table fluctuations are still incomplete, particularly in confined carbonate systems. This limitation is increasingly relevant as extreme precipitation intensifies under climate change, raising the frequency of large recharge events.

Southern Spain experienced an exceptional and sustained rainfall episode in early 2026, with cumulative precipitation locally exceeding three times the seasonal average. This hydrological anomaly resulted in a rapid and pronounced rise in groundwater levels within a regional carbonate aquifer and coincided with a sequence of shallow earthquakes (Fig. 1).

Here we show that extreme aquifer recharge can generate pore-pressure perturbations sufficient to trigger seismicity within a confined karst system. Using this well-constrained natural example, we integrate structural, hydrogeological and seismic observations to link earthquake occurrence to the spatio-temporal evolution of groundwater pressure.

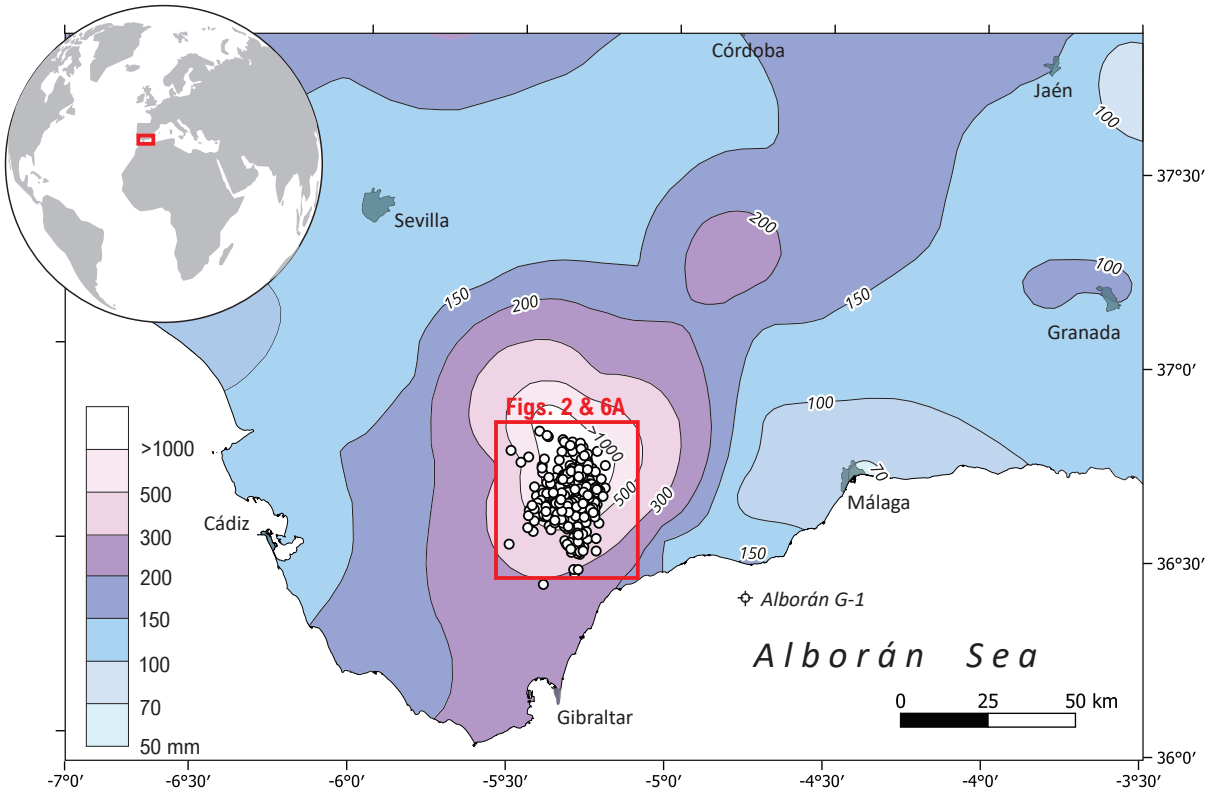

Fig. 1. Spatial distribution of cumulae rainfall across southwestern Spain during February 2026. Colours represent total precipitation, and cicles indicate epicentres. The locaation of the 3Deological model (Fig. 2), the earthquake heat map (Fig 6A) and the Alborán G-1 borehole are also shown.

2. Data and Methods

The distribution map of cumul ate rainfall during February 2026 was derived from regional meteorological stations overing the Grazalema-Líbar ranges (AEMET, 2026) (Fig. 1). Groundwater levels within the Líbar carbonate aquifer were constrained using a combination of hitorical monthly measurements and high-frequency monitoring data. From 9 February onward, an automated sensor installed at the Molino del Santo control spring (Benaoján station) ecorded discharge at 15-minute intervals, allowing detailed characterization of shor-term hydrological responses to recharge events.

Piezometric variations ere independently monitored at the Jimera de Líbar control piezometer, located near the central sector of the aquifer. This site provides daily measurements and was intensively surveyed from 11 February onward, immediately following peak precipitation, to constrain the maximum hydraulic response of the system.

The geological framework is based on detailed cross-sections, a 3D geological model, field-based structural measurements, and fracture mapping derived from high-resolution satellite imagery. The model integrates stratigraphic boundaries, fold geometry, and regional thrust architecture. Fracture systems within the carbonate aquifer were characterized in terms of orientation, density, and connectivity in order to assess potential fluid-flow pathways. The 3D model, constructed using Move™ Suite, provides a kinematically consistent structural framework linking earthquake distribution to fault geometry, fracture connectivity, and aquifer confinement.

Seismicity associated with the February–March 2026 sequence was analysed using the relocated earthquake catalogue released by the Instituto Geográfico Nacional (IGN) in a public Zenodo repository (Lozano, 2026). The dataset includes earthquakes occurring between 3 February 2026 and 1 March 2026 with magnitudes ≥ 1.5, relocated by the IGN using a two-step procedure in which absolute locations were first obtained with NonLinLocTM using the velocity model of El Moudnib et al. (2015), and subsequently refined through relative relocation with HypoDDTM to improve spatial clustering and depth resolution. Full details of the relocation procedure and dataset are provided in Lozano (2026). Moment tensor solutions were obtained from the IGN and follow the methodology of Rueda and Mezcua (2005).

The temporal evolution of seismicity was analysed using daily earthquake counts in comparison with precipitation and groundwater-level time series to identify temporal correspondence and estimate delays between hydrological forcing and seismic response. The relationship between shallow (<4 km) and deep (4–15 km) seismicity was further quantified using cross-correlation analysis to determine the time lag that maximizes correlation between both depth domains.

Hydrologically induced stress changes were evaluated using a MATLAB-based fracture analysis toolbox to compute slip tendency, reactivation potential, and Mohr–Coulomb failure conditions under variable effective stress (Healy et al., 2017). Pressure perturbations derived from groundwater-level variations were superimposed onto the regional stress field to assess the likelihood of fault reactivation.

The spatio-temporal evolution of pore pressure was modelled using the one-dimensional diffusion equation, following Talwani and Acree (1984). Pressure propagation away from a recharge boundary is described by:

$$p(z,t) = p0\ erfc\left(\frac{Z}{2\sqrt{at}}\right)$$

Where $p0$ the initial pressure perturbation, z is distance, t is time, α is hydraulic diffusivity and *erfc* is the complementary error function. Modelled pressure fields were compared with relocated seismicity to evaluate the spatio-temporal coherence between pore-pressure diffusion and earthquake occurrence.

3. Results

3.1. Karst structure and hydrology

Seismicity is concentrated within Mesozoic carbonate units of the Sierra de Líbar within the Western Betic Cordillera which forms part of the Gibraltar Arc (southern Spain).

The stratigraphic succession comprises Upper Triassic evaporites and shales that act as a regional basal aquitard (Fig. 2), overlain by highly fractured Lower to Middle Jurassic carbonates forming a laterally continuous aquifer, capped by low-permeability Cretaceous and Miocene units. The structure comprises three stacked thrust sheets: an upper sheet formed by Internal Zone units, an intermediate sheet hosting the Sierra de Líbar monocline and a partially confined carbonate aquifer, and a lower sheet in which Jurassic carbonates are largely buried beneath low-permeability units (Fig. 2).

Earthquakes are primarily located within the intermediate thrust sheet that contains the Sierra de Líbar aquifer, encompassing unconfined sectors and the confined domain beneath the metamorphic thrust hanging wall (Figs. 2 and S1). The carbonates are pervasively fractured, forming a dense, well-connected network. The dominant family is oriented ~N130°. Most events cluster within this domain, with fewer earthquakes occurring in the lower carbonate thrust sheet and only rare events in the basement near major thrusts. In map view, the Jurassic carbonates form a regionally connected karst aquifer draining towards the Guadiaro River. Spring elevations decrease from ~440 m to ~240 m, defining a south-southwest hydraulic gradient.

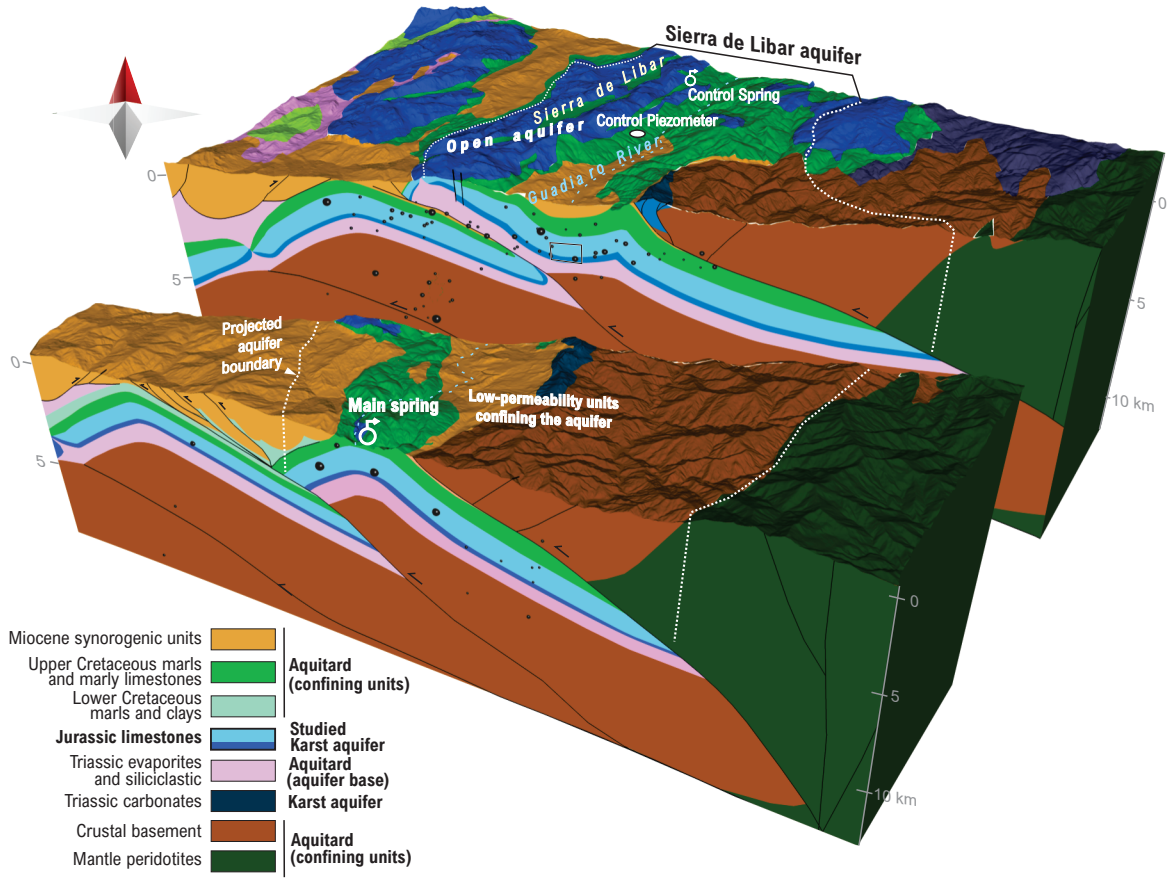

Fig. 2. Oblique view of the 3D geological model of the Sierra de Líbar aquifer, illustrating the structural framework of the carbonate system. Jurassic carbonates form a laterally continuous karst aquifer that becomes locally confined beneath low-permeability Cretaceous and Miocene units. Earthquake hypocentres are projected onto the cross-sections, highlighting their distribution within the aquifer. The locations of the main springs and the control piezometer are indicated.

3.2. Hydro-seismic response to the late 2025 - early 2026 recharge event

Between 13 November 2025 and 12 February 2026, total precipitation reached 3186.8 mm at the Grazalema station. Figure 3 illustrates the temporal evolution of precipitation, groundwater response, and seismicity during first months of 2026. Precipitation increased markedly from mid-January, reaching a maximum daily value on 4 February, with cumulative rainfall accelerating during the last week of January and early February (Fig. 3, bottom panel).

The hydrological response of the Sierra de Líbar aquifer was exceptional. An initial recharge pulse (313.2 mm over five days) increased discharge at the Molino del Santo spring from ~6–7 m^3/s to ~25–30 m^3/s (Fig. 3, middle panel). Discharge subsequently decreased but remained elevated at ~15–20 m^3/s until late January. A subsequent 22-day rainfall period delivered 2323.8 mm,

culminating in an extreme daily precipitation of 553.9 mm on 4 February. Maximum discharge was reached on 5 February, when values peaked at ~45 m³/s, followed by a progressive recession during the second half of February and early March.

Groundwater levels recorded at the Jimera de Líbar control piezometer (Fig. 3, top panel) show an exceptional rise of ~79 m, with values remaining consistently above the spring elevation. This rise and fall closely mirrors the discharge evolution.

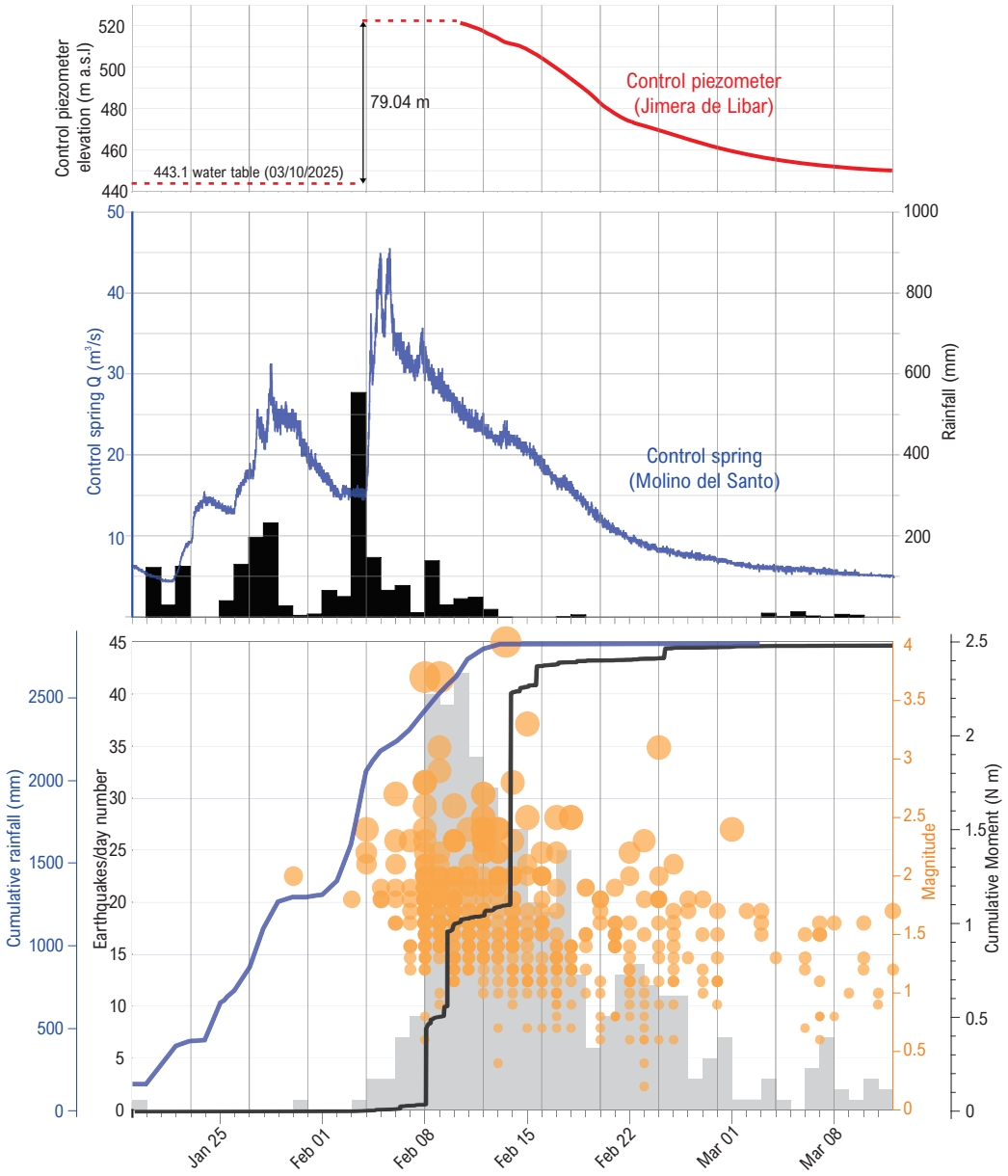

Fig. 3. Temporal evolution of precipitation, groundwater levels and seismicity during the 2026 recharge event. Groundwater levels (top) show an exceptional ~80 m rise. Spring discharge and rainfall (middle) illustrate the rapid hydrological response. Cumulative rainfall, earthquake counts, magnitudes and cumulative seismic moment (bottom) show that seismicity intensifies shortly after peak recharge, with most seismic energy released over a short interval.

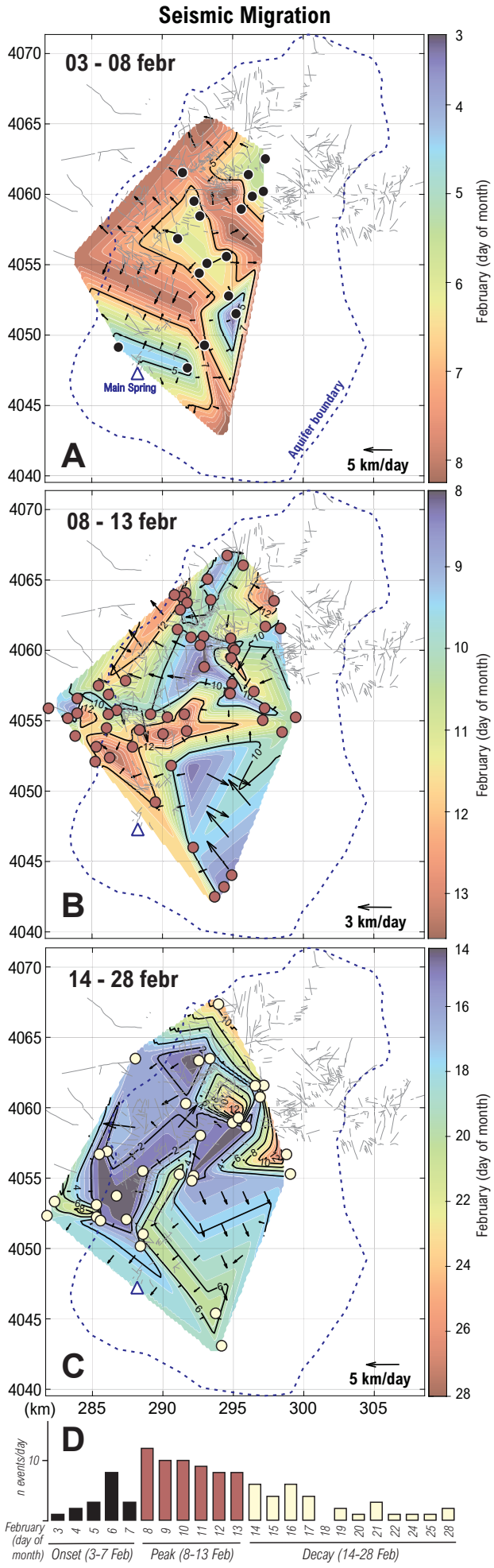

Seismic activity intensified shortly after the hydrological peak. The highest number of earthquakes was recorded on 8 February, approximately three days after maximum discharge and four days after peak daily precipitation. This short temporal lag suggests a close temporal link between hydrological forcing and seismicity. This interpretation is further supported by the longer-term record, which shows that more modest groundwater fluctuations, well below the 2026 peak, do not systematically trigger seismicity (Fig. S2).

The cumulative seismic moment increased sharply between 8 and 15 February (Fig. 3, bottom panel), indicating that most seismic energy was released over a short interval following peak recharge conditions. The sequence is dominated by small-magnitude events (mostly M < 2), with a few earthquakes near Mw ~4.0 and no dominant mainshock, consistent with swarm-like behaviour.

Earthquakes are predominantly shallow, with most hypocentres located above 4 km depth, although deeper events represent approximately one third of the sequence. Seismicity evolves through three phases—onset, peak and decay—as reflected by their temporal clustering and spatial distribution (Figs. 3 and 4).

Fig. 4. Spatio-temporal migration of seismicity throughout the sequence. (A–C) Spatial distribution of relocated earthquakes (0–4 km depth) for the three phases: onset (3–7 February; A), peak (8–13 February; B), and decay (14–28 February; C). Event colours correspond to the phase classification shown in panel D. During the onset phase, seismicity initiates from a localized sector and propagates as a coherent front. At peak activity, the distribution becomes more widespread and multidirectional, reflecting activation of a broader fracture network. During the decay phase, seismicity becomes more diffuse and extends toward the periphery, indicating redistribution of activity across the system. This evolution reflects a transition from localized propagation to distributed seismic activation within a hydraulically connected fracture network. (D) Daily earthquake counts defining the onset, peak and decay phases.

During the onset phase, seismicity initiates within a localized, confined sector of the aquifer and propagates as a coherent front. Peak activity is more spatially distributed and multidirectional, whereas during the decay phase migration becomes outward-directed from the central cluster, extending into the unconfined aquifer and toward the periphery (Fig. 4).

3.3. Long-term hydro-seismic variability

The temporal evolution of precipitation, groundwater levels, stress perturbations and seismicity during a record of 20 years is shown in Fig. 5. Groundwater levels closely follow precipitation pulses, indicating a rapid hydrological response of the karst aquifer. These variations generate transient pore-pressure perturbations (ΔP), superimposed on a progressively increasing tectonic stress field. Seismicity clusters during periods of enhanced hydrological forcing, particularly during the most intense recharge episodes, notably in 2010, 2013, 2018 and 2026.

The relationship between precipitation and seismicity was further analysed using extended rainfall records and earthquake catalogues more than three decades (1985–2026) (Fig. S2). Precipitation shows strong interannual variability, with several high-magnitude rainfall years distributed throughout the record. To evaluate the role of extreme events, years exceeding the 95th percentile of annual precipitation were identified. Although not all extreme rainfall years are associated with seismicity, the highest levels of earthquake activity are restricted to these events, with the 2026 episode representing a clear outlier. However, seismicity does not exhibit a consistent response to these fluctuations, and most years with moderate to high precipitation are not associated with increased earthquake activity.

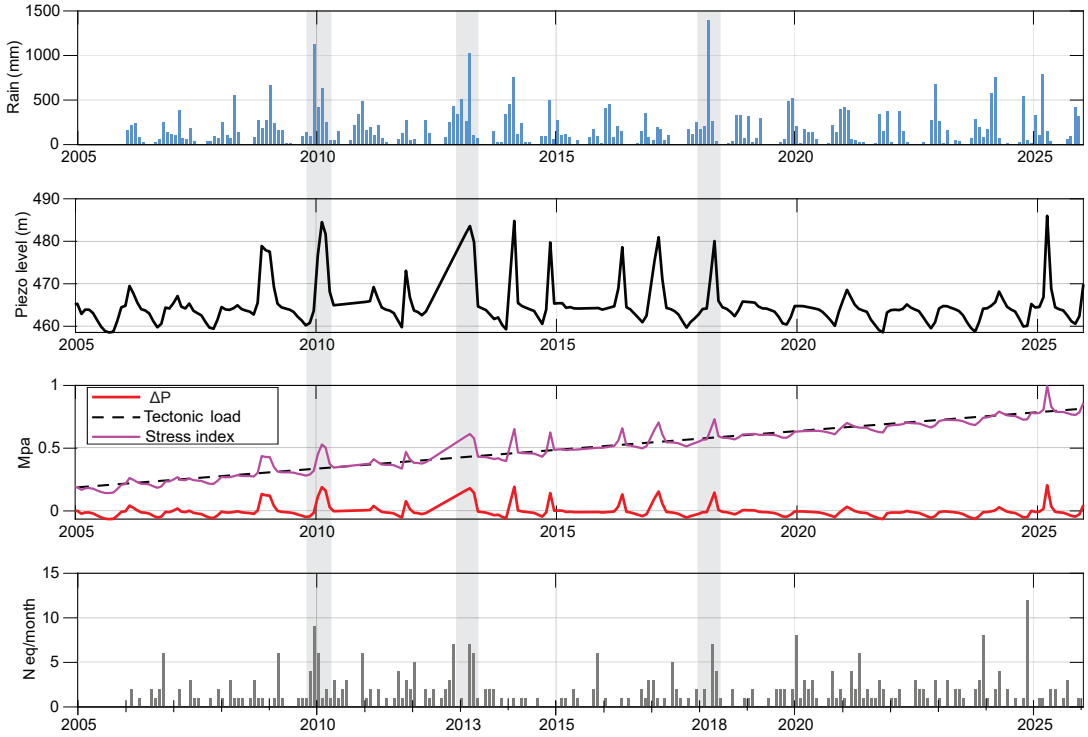

Fig. 5. Monthly evolution of precipitation, piezometric level, pore-pressure change (ΔP), tectonic loading, and seismicity excluding the 2026 swarm. Precipitation (top panel) corresponds to the Grazalema meteorological station. The piezometric record (second panel) represents groundwater level variations in the Líbar aquifer. The third panel shows estimated pore-pressure changes (ΔP, red), cumulative tectonic loading (black dashed line) derived from GNSS strain rates (~0.8 nanostrain yr^{-1}; equivalent to ~0.03 MPa yr^{-1}; Madarieta-Txurruka et al., 2025), and the resulting stress index (magenta). The fourth panel shows monthly earthquake counts within the study area (36.2°–36.9° N, −5.7° to −4.8° W). Shaded intervals highlight periods of increased hydrological input. The absence of a systematic correspondence between groundwater fluctuations and seismicity contrasts with the pronounced response observed during the 2026 extreme recharge event (not shown for scaling reasons), supporting a threshold-controlled triggering mechanism.

3.4. Stress perturbation modelling within the aquifer

Stress perturbations were evaluated using the orientation and connectivity of the fracture network within the carbonate aquifer (Fig. 6), focusing on the seismogenic interval at ~2.5 km depth.

The regional stress field is constrained independently. Wellbore breakout data from the Andalucía G-1 borehole indicate SHmax = 98 ± 4 MPa (1.3-3.1 km) (Fernández-Ibáñez et al., 2007). At 2.5 km, vertical stress is ~65 MPa assuming a lithostatic gradient of 25-27 MPa km^{-1}. Baseline pore pressure is hydrostatic (~25 MPa), with recharge inducing an additional ΔP ≈ 0.8 MPa from the observed ~80 m piezometric rise. Assuming μ = 0.6, the minimum horizontal stress compatible with near-critical failure is ~50 MPa, yielding a stress tensor consistent with breakout constraints and Byerlee friction

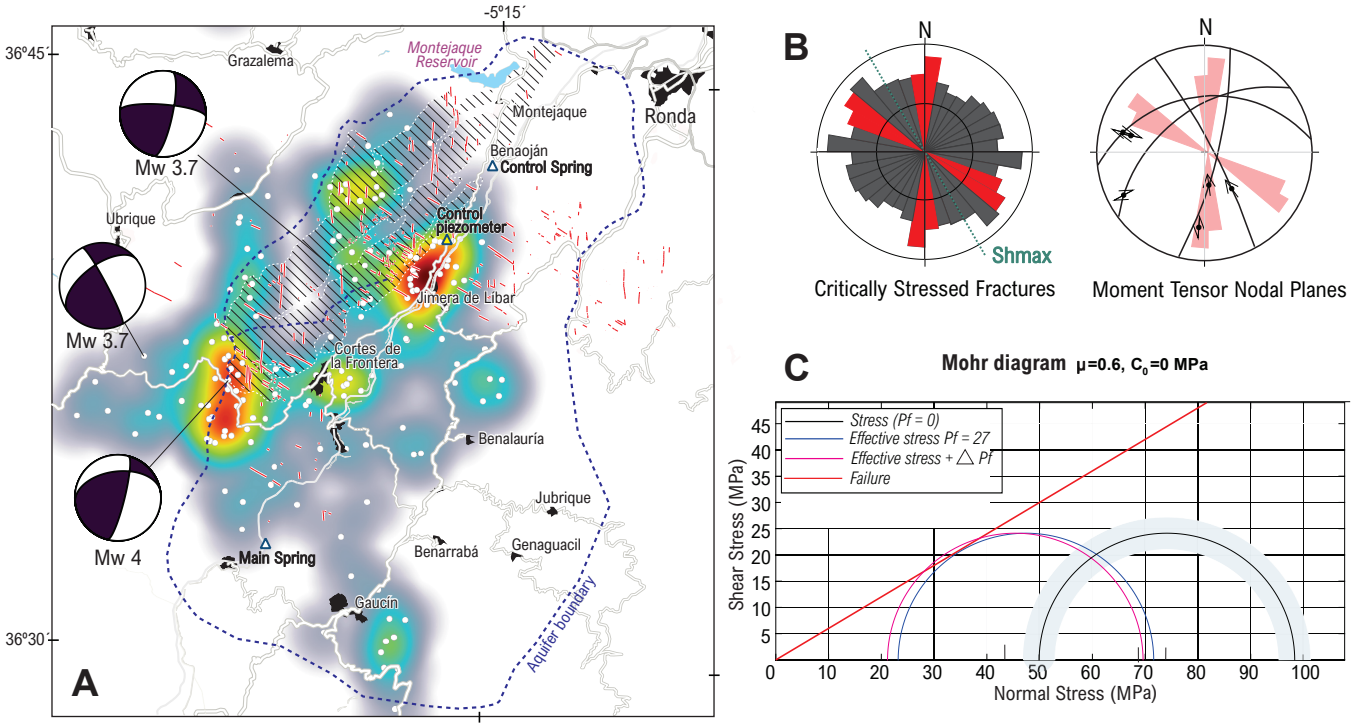

Fig. 6. Geomechanical controls on the February 2026 seismic swarm. (A) Heat map of earthquake occurrence within the Sierra de Líbar aquifer. Most events cluster in the confined sector, whereas the unconfined aquifer (hatched area) shows lower activity. Fracture traces are shown, with segments predicted to be critically stressed under the regional stress field highlighted. (B) Rose diagrams of mapped fracture orientations. Critically stressed fractures are shown in red. Nodal planes of the three focal mechanisms align with these orientations. SHmax indicates the regional maximum horizontal stress direction. (C) Mohr-Coulomb diagram illustrating the effect of recharge-induced pore-pressure increase.

(σ1 = 98 MPa, σ2 = 65 MPa, σ3 = 50 MPa).

GNSS strain rates (~0.8 nanostrain yr^{-1}) (Madarieta-Txurruka et al., 2025) correspond to differential stress accumulation of ~0.03 MPa yr^{-1}, indicating that the observed pore-pressure increase is mechanically equivalent to several decades of tectonic loading. Slip tendency analysis shows that only a subset of optimally oriented fractures approaches failure under baseline conditions, whereas recharge reduces effective normal stress and selectively promotes slip (Fig. 6C). Failure is thus restricted to favourably oriented fractures, consistent with swarm-like seismicity and the absence of large ruptures.

Pore-pressure diffusion and seismicity frequency was represented in a 3D graph as a function of time and distance following Talwani and Acree (1984) formulations (Fig. 7). Earthquakes cluster at locations where pressure perturbations reach ~0.4–0.7 MPa, indicating that seismicity is governed by pore-pressure diffusion within a critically stressed fracture network and providing quantitative constraints on the effective hydraulic diffusivity of the system.

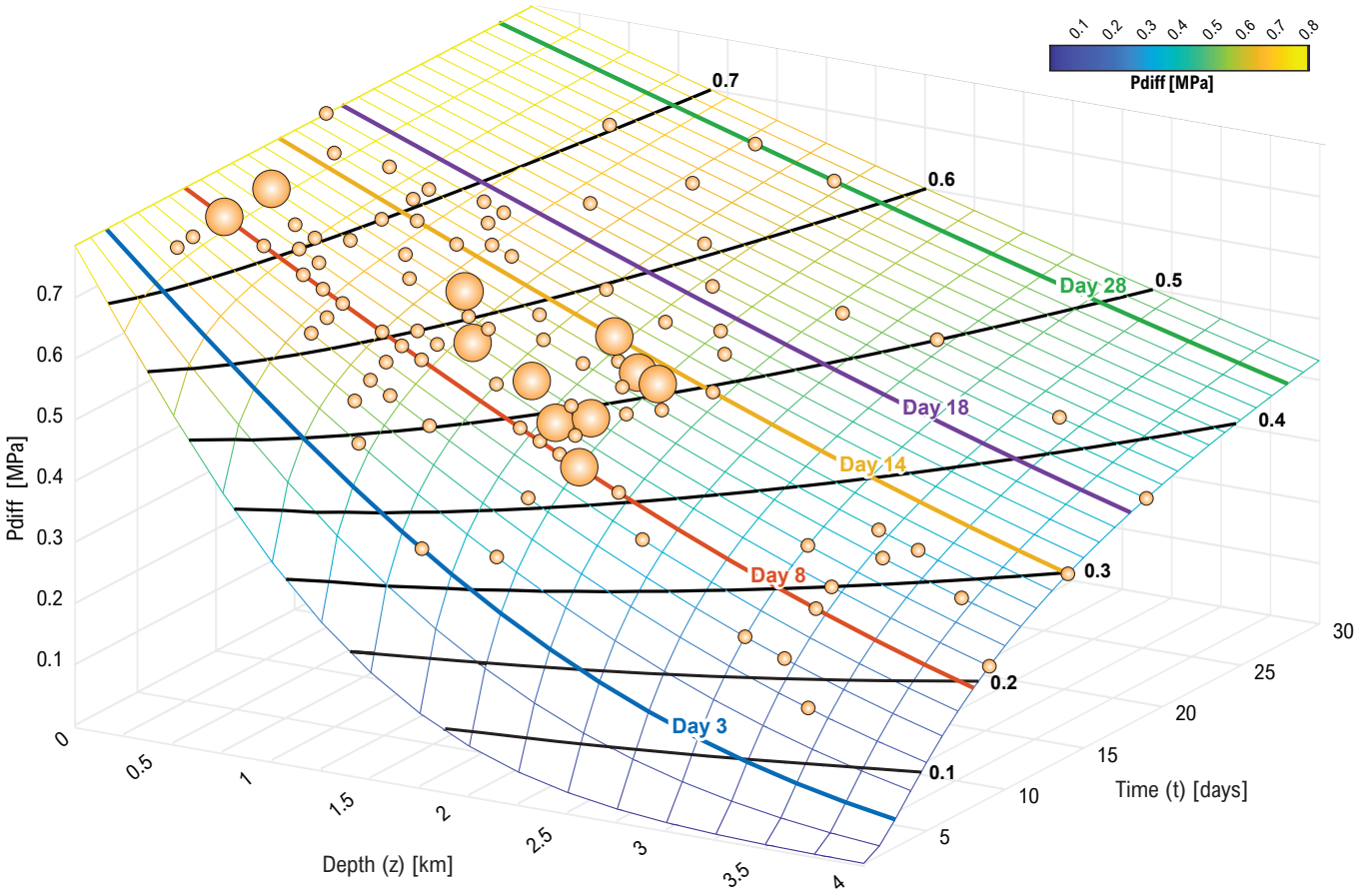

Fig. 7. Pore-pressure diffusion model as a function of time and distance. The coloured surface shows pressure perturbations (ΔP, MPa), with time contours indicating pressure-front propagation. Circles represent relocated earthquakes (0–4 km depth), with size proportional to the number of events. Seismicity clusters at ΔP ~0.4–0.7 MPa, consistent with diffusion-controlled triggering in a critically stressed fracture network.

3.5. Temporal relationship between aquifer and basement seismicity

Figure 8 summarizes the temporal evolution of rainfall forcing, hydrological response, and seismicity during the February 2026 sequence. Precipitation and antecedent precipitation index (API) show a progressive increase leading up to the onset of seismicity, indicating sustained hydrological loading of the system (Fig. 8A).

Seismicity is distributed within two depth domains: a shallow population (<4 km) associated with the carbonate aquifer, and a deeper population (4–15 km) located within the underlying basement. The depth-time distribution reveals a systematic migration pattern following swarm onset (Fig. 8B). Diffusion fronts for hydraulic diffusivities of 11 and 18 $m^2 s^{-1}$ are superimposed for reference. The two populations exhibit distinct temporal behaviour (Fig. 8C). Shallow seismicity dominates the early

phase of the sequence and reaches peak activity shortly after swarm initiation. In contrast, deeper events within the basement are less numerous and occur later displaying a more gradual and sustained temporal evolution.

This delay in seismic response was tested applying a shift to the deep seismicity time series (Fig. 8D). After correction for a lag of 4 days, the deep events synchronize the shallow-ones, suggesting a systematic delay between the two populations.

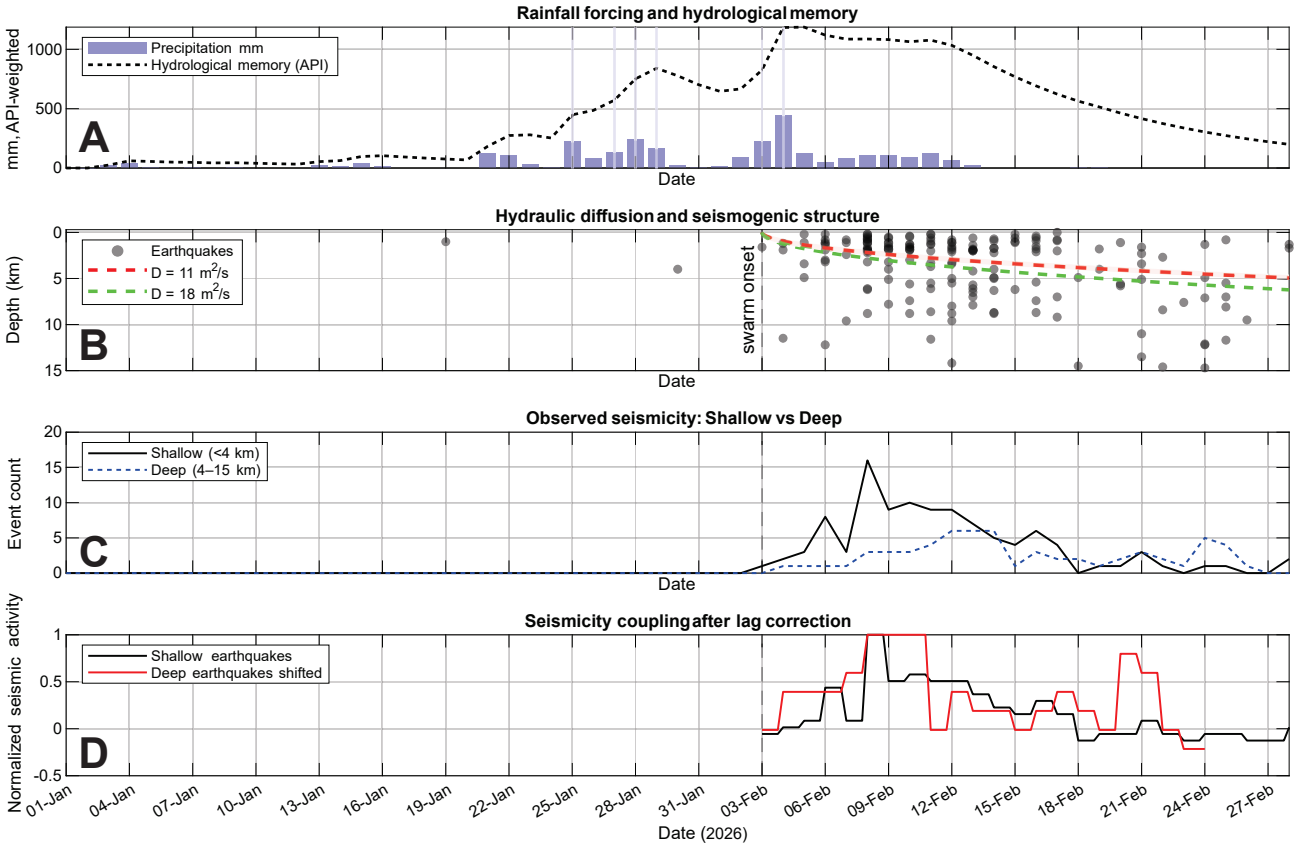

Fig. 8. Relationship between shallow aquifer-hosted seismicity and deeper basement seismicity during the February 2026 sequence. (A) Daily precipitation at the Grazalema station and antecedent precipitation index (API), showing the progressive hydrological loading preceding swarm onset. Vertical lines mark major rainfall pulses. (B) Depth–time distribution of relocated earthquakes. Seismicity is organized into two depth domains: a shallow population (<4 km) associated with the Líbar karst aquifer and a deeper population (4–15 km) located within the underlying basement. Dashed curves show diffusion fronts calculated for hydraulic diffusivities of 11 and 18 $m^2 s^{-1}$. The shaded band indicates the uncertainty envelope around the preferred diffusion model. (C) Daily earthquake counts for shallow and deep seismicity. Shallow earthquakes dominate the early phase of the sequence, whereas deeper events show a more delayed and sustained temporal evolution. (D) Normalized shallow seismicity and deep seismicity shifted by the best-fit lag. After applying a lag correction of ~4 days, the deep seismicity more closely parallels the temporal evolution of the shallow sequence, highlighting a systematic delay between both populations.

4. Discussion

4.1. Evidence for hydrological control on seismicity

The February-March 2026 seismic sequence may reflect either a purely tectonic swarm or a response to transient hydrological forcing. Discriminating between these mechanisms is critical for understanding earthquake nucleation in the study area.

Seismicity is dominated by shallow events (<4 km), spatially confined to the carbonate units of the Sierra de Líbar aquifer. The sequence is characterized by the absence of a mainshock, with seismicity distributed across the aquifer in map and section view rather than localized along a major fault (Figs. 2, S1). Such spatial dispersion is difficult to reconcile with a purely tectonic origin and instead points to aquifer-scale pore-pressure redistribution within a connected fracture network (Figs. 6 and 9). Deeper earthquakes that occur within the underlying basement indicate other type of response, possibly mechanically triggered as will be discussed in section 4.5. In this framework, the temporal relationship between precipitation, groundwater response and seismicity becomes a key diagnostic.

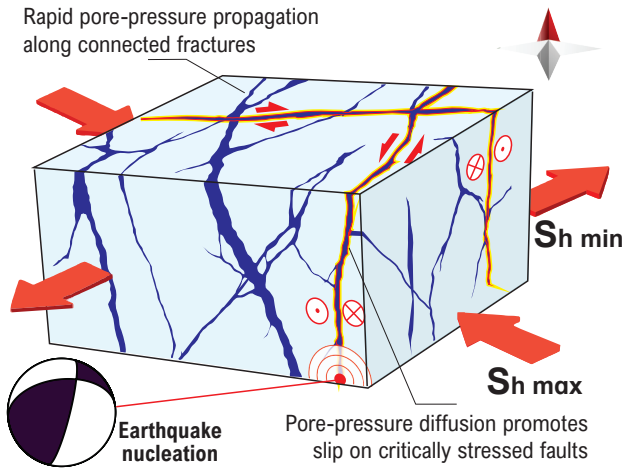

Fig. 9. Conceptual representation of the fractured karst aquifer, illustrating pore-pressure diffusion through a connected fracture network, reduction of effective normal stress, and slip on critically stressed faults, consistent with the observed seismicity.

4.2. Hydrological triggering of seismicity in a critically stressed crust

The close temporal and spatial coupling between extreme recharge and the burst of shallow seismicity indicates that hydrological forcing acted as the immediate trigger within a tectonically loaded crust. While regional convergence across the Gibraltar Arc provides long-term stress accumulation, hydrological forcing reduces effective normal stress on favourably oriented pre-existing fractures, promoting strike-slip faulting (Fig. 9).

Independent constraints from wellbore breakouts, GNSS strain rates and lithostatic loading indicate that the carbonate reservoir operates near frictional equilibrium at seismogenic depths. Under these conditions, even modest pore-pressure increases can advance failure. The ~80 m groundwater rise associated with the 2026 recharge event corresponds to a pressure increase of ~0.8 MPa—small in absolute terms, yet mechanically significant for faults already close to failure (Scholz, 2010). This perturbation is equivalent to several decades of tectonic stress accumulation, highlighting the capacity of extreme hydrological events to modulate earthquake recurrence times.

4.3. Diffusion-driven pressure propagation and confinement

The temporal and spatial evolution of the seismic sequence is consistent with the progressive propagation of pore-pressure perturbations within the aquifer (Fig. 9). The transition from nucleation fronts during the onset phase to widespread seismicity during peak conditions and to spatially diffuse seismicity during the decay stage (Fig. 4) can be understood by the progressive activation, diffusion and subsequent relaxation of hydraulic pressure in the fractures. Seismic migration patterns show a well-defined propagation front during the onset phase, consistent with diffusion-controlled pressure increase, followed by more complex and multidirectional propagation at peak activity. This evolution reflects a shift from localized overpressure to distributed activation across the fracture network.

During the decay phase, migration becomes outward-directed from the central cluster, extending toward both confined peripheral sectors and adjacent unconfined domains. This pattern reflects lateral redistribution of pore pressure and pressure relaxation following peak recharge.

4.4. Threshold-controlled behaviour and implications

Moderate recharge episodes may occasionally coincide with periods of seismicity; however, neither precipitation, pore-pressure increases, nor earthquake occurrence reach the levels observed during the extreme 2026 event. Instead, the observations support a threshold-controlled behaviour, in which the system remains largely insensitive to typical groundwater fluctuations and is only activated when pore-pressure plus the regional stress accumulation perturbations exceed a critical level. The clustering of earthquakes within a narrow range of pressure increase (~0.4–0.7 MPa), together with the disproportionate response to the 2026 event, supports the existence of such a threshold.

This behaviour contrasts with regions where seismicity appears to vary more continuously with hydrological loading (e.g., Bettinelli et al., 2008), but is consistent with episodic triggering associated with karst recharge (Bragato, 2021). In confined carbonate systems, hydrological forcing may therefore remain largely ineffective until a critical pressure condition is reached. As climate change intensifies extreme precipitation events, hydrologically driven stress transients may increasingly influence shallow seismicity in globally distributed carbonate mountain belts.

4.5. Mechanical coupling between aquifer and basement seismicity

An intriguing feature of the earthquake swarm is the location of several events in the basement, offering insights into processes operating beyond the hydrologically active layer.

The temporal evolution of the sequence reveals a systematic delay of approximately four days between shallow and deep seismicity (Fig. 8). This offset indicates that earthquake occurrence in the basement does not initiate synchronously with the hydrologically driven activity within the aquifer. The observed delay is short compared to the timescales of months-years expected for direct pore-pressure diffusion to depths of 9-15 km (e.g. Major et al., 1998), particularly given the presence of low-permeability units separating the aquifer from the basement. This makes a direct hydraulic connection unlikely. At the same time, the delay is inconsistent with instantaneous elastic triggering from a single shallow event, which would be expected to produce a near-synchronous response. Instead, the observations support progressive mechanical coupling between the two depth domains which can be interpreted as separate failure regimes: a shallow population (<4 km) with low effective stress due to the increase in pore pressure within the carbonate aquifer, and a deeper population (4–15 km) within the basement, with no direct hydraulic connection to the aquifer.

Hydrologically induced seismicity within the aquifer redistributes stress in the upper crust, and its cumulative effect promotes failure on critically stressed basement structures. The delayed onset of few days of deeper events reflects the time required for stress perturbations to build up. These results define a fast coupled system in which hydrological forcing initiates shallow seismicity, while deeper earthquakes represent the mechanical response of the crust.

5. Conclusions

Extreme recharge of a confined karst aquifer in southern Spain triggered a swarm of shallow earthquakes, providing a well-constrained natural example of hydrologically induced seismicity. The temporal and spatial evolution of the sequence demonstrates that transient pore-pressure perturbations can effectively promote failure in a critically stressed crust, despite their relatively small magnitude.

Seismicity is not continuously modulated by hydrological variability but is restricted to periods of enhanced recharge, with most groundwater fluctuations failing to trigger earthquakes, suggesting threshold-controlled behaviour. The 2026 event stands out within the long-term record as an exceptional case in which pore-pressure increases were sufficient to activate a large number of fractures.

The seismic sequence within the aquifer evolves through a characteristic three-stage pattern, from localized nucleation to distributed activation and subsequent outward migration, consistent with pore-pressure diffusion within a laterally connected fracture network. Structural confinement favours pressure accumulation and delayed dissipation, allowing confined karst systems to act as transient stress modulators. More importantly, deeper seismicity within the basement reflects a mechanically driven response promoted by shallow seismicity. This delayed response, by approximately four days, is consistent with stress transfer rather than direct fluid processes.

As extreme precipitation events intensify under climate change, hydrologically driven stress perturbations may become an increasingly important control on shallow seismicity in carbonate mountain belts.

Acknowledgements

This work was carried out by the Tectonic Processes and GeoResources Research Group (IGME-CSIC) and supported by projects H2RISE, PID2024-161600OB-I00 and AQUA-KARST (PLSQ-2023–00284). We sincerely thank Lucía Lozano (Instituto Geográfico Nacional, IGN) for providing the earthquake relocations, and Sandra Ruiz, Beatriz Gaite and Juan Vicente Cantavella (IGN) for insightful discussions that greatly contributed to this work.

Data availability

Earthquake catalogues used in this study are publicly available from the Instituto Geográfico Nacional (IGN, Spain) seismic database (https://www.ign.es; Instituto Geográfico Nacional, 2026). The relocated hypocentre dataset used here was produced and released independently by the IGN and is publicly available through Zenodo (Lozano, 2026; https://doi.org/10.5281/zenodo.19570477). Precipitation data were obtained from the Agencia Estatal de Meteorología (AEMET, Spain), including the Grazalema meteorological station records used in this study. Groundwater level and discharge data were provided by the Demarcación Hidrográfica de las Cuencas Mediterráneas Andaluzas (DHCMA). All other data supporting the findings of this study are available from the corresponding author upon reasonable request.

Author contributions

A.P. and J.G.-S. conceived the study, developed the conceptual framework, and led data analysis and manuscript writing. A.G.-R. Contributed hydrogeological data acquisition and analysis. J.M.G.-F. Contributed to hydrogeological data analysis. A.R.-C. Reviewed and edited the manuscript. S.M.-R. Contributed hydrogeological data acquisition and participated in manuscript revision. All authors discussed the results and contributed to the final manuscript.

Agencia Estatal de Meteorología (AEMET), 2026. Avance climatológico mensual: febrero de 2026 en Andalucía, Ceuta y Melilla. Public report, March 2026.

Bettinelli, P., Avouac, J.-P., Flouzat, M., Bollinger, L., Ramillien, G., Rajaure, S., et al., 2008. Seasonal variations of seismicity and geodetic strain in the Himalaya induced by surface hydrology. Earth Planet. Sci. Lett. 266, 332–344. https://doi.org/10.1016/j.epsl.2007.11.021

Bragato, P.L., 2021. Systematic triggering of large earthquakes by karst water recharge: Statistical evidence in northeastern Italy. Front. Earth Sci. 9, 1–11.

El Moudnib, L., et al., 2015. Crustal structure of the Betic–Rif system, western Mediterranean, from local earthquake tomography. Tectonophysics 643, 94–105.

Fernández-Ibáñez, F., Soto, J.I., Zoback, M.D., Morales, J., 2007. Present-day stress field in the Gibraltar Arc (western Mediterranean). J. Geophys. Res. 112, B08404. https://doi.org/10.1029/2006JB004683

Hainzl, S., Kraft, T., Wassermann, J., Igel, H., Schmedes, E., 2006. Evidence for rainfall-triggered earthquake activity. Geophys. Res. Lett. 33, L19303. https://doi.org/10.1029/2006GL027642

Healy, D., et al., 2017. FracPaQ: A MATLAB™ toolbox for the quantification of fracture patterns. J. Struct. Geol. 95, 1–16. https://doi.org/10.1016/j.jsg.2016.12.003

Hsu, Y.-J., et al., 2025. Hydrologically-induced crustal stress changes and their association with seismicity rates in Taiwan. Earth Planet. Sci. Lett. 651, 119181.

Husen, S., Bachmann, C., Giardini, D., 2007. Locally triggered seismicity in the central Swiss Alps following the large rainfall event of August 2005. Geophys. J. Int. 171, 1126–1134. https://doi.org/10.1111/j.1365-246X.2007.03561.x

Instituto Geográfico Nacional (IGN), 2026. Catálogo de terremotos. https://doi.org/10.7419/162.03.2022

Jiménez, M.-J., García-Fernández, M., 2000. Occurrence of shallow earthquakes following periods of intense rainfall in Tenerife, Canary Islands. J. Volcanol. Geotherm. Res. 103, 463–468.

Kraft, T., Wassermann, J., Schmedes, E., Igel, H., 2006. Meteorological triggering of earthquake swarms at Mt. Hochstaufen, SE-Germany. Tectonophysics 424, 245–258.

Lozano, L., 2026. Relocated hypocenters of the February 2026 seismicity in SW Betic Cordillera (South Spain) [dataset]. Zenodo. https://doi.org/10.5281/zenodo.19570477

Madarieta-Txurruka, A., et al., 2026. New insights on active geodynamics of Iberia and Northwestern Africa from seismic stress and geodetic strain-rate fields. Gondwana Res. 149, 314–336.

Major, J.J., Iverson, R.M., Costain, J.K., Bollinger, G.A., Speer, A. 1998. Comment and Reply on "Hydroseismicity—A hypothesis for the role of water in the generation of intraplate seismicity". Geology, 16 (6), 562–564. https://doi.org/10.1130/0091-7613(1988)016<0562:CAROHA>2.3.CO;2

Rueda, J., Mezcua, J., 2005. Near-real-time seismic moment-tensor determination in Spain. Seismol. Res. Lett. 76, 455–465.

Saar, M.O., Manga, M., 2003. Seismicity induced by seasonal groundwater recharge at Mt. Hood, Oregon. Earth Planet. Sci. Lett. 214, 605–618. https://doi.org/10.1016/S0012-821X(03)00418-7

Scholz, C.H., 2010. The Mechanics of Earthquakes and Faulting, 2nd ed. Cambridge Univ. Press, Cambridge.

Shapiro, S.A., Patzig, R., Rothert, E., Rindschwentner, J., 2003. Triggering of seismicity by pore-pressure perturbations: Permeability-related signatures of the phenomenon. Pure Appl. Geophys. 160, 1051–1066.

Talwani, P., Acree, S., 1984. Pore pressure diffusion and the mechanism of reservoir-induced seismicity. Pure Appl. Geophys. 122, 947–965.

Tarantino, S., et al., 2024. Non-linear elasticity, earthquake triggering and seasonal hydrological forcing along the Irpinia fault, Southern Italy. Nat. Commun. 15, 9821. https://doi.org/10.1038/s41467-024-54094-4

Wang, C.-Y., Manga, M., 2021. Water and Earthquakes. Springer, Cham.

Wolf, L.W., Rowe, C.A., Horner, R.B., 1997. Periodic seismicity near Mt. Ogden on the Alaska–British Columbia border: A case for hydrologically triggered earthquakes? Bull. Seismol. Soc. Am. 87, 1473–1483. https://doi.org/10.1785/bssa0870061473

Supplementary Material

Fig. S1. Geological cross-sections and projected seismicity across the Sierra de Líbar karst aquifer. (A–C) NW-SE geological cross-sections showing the structural architecture of the carbonate aquifer within the Western Betic Cordillera. The sections illustrate stacked thrust sheets, folded Mesozoic carbonate units, and overlying low-permeability formations that locally confine the aquifer. The Jurassic carbonate unit forms a laterally continuous karst aquifer bounded by Triassic evaporites at the base and Cretaceous–Miocene units acting as a regional aquitard. Relocated earthquakes are projected onto each section within a ±3 km swath and plotted as circles scaled by magnitude. Seismicity is predominantly concentrated within the carbonate aquifer and along its boundaries, with fewer events in the underlying units and basement.

Fig. S2. Long-term variability of precipitation and seismicity in the study area. Annual precipitation recorded at the Grazalema station is shown together with the number of earthquakes within the study region (36.2°–36.9° N, −5.7° to −4.8° W). Grey shading highlights years exceeding the 95th percentile (P95) of precipitation. While precipitation exhibits strong interannual variability, seismicity does not show a systematic response, although the highest earthquake activity is restricted to years of extreme rainfall, most notably the 2026 event